www.sciencemag.org/cgi/content/full/science.aah6114/DC1

Supplementary Materials for

Time-resolved x-ray absorption spectroscopy with a water window high-harmonic source

Yoann Pertot, Cédric Schmidt, Mary Matthews, Adrien Chauvet, Martin Huppert, Vit Svoboda, Aaron von Conta, Andres Tehlar, Denitsa Baykusheva, Jean-Pierre Wolf, Hans Jakob Wörner*

*Corresponding author. E-mail: hwoerner@ethz.ch

Published 5 January 2017 on *Science* First Release
DOI: 10.1126/science.aah6114

This PDF file includes:

Contents

Text S1 **Experimental setup**

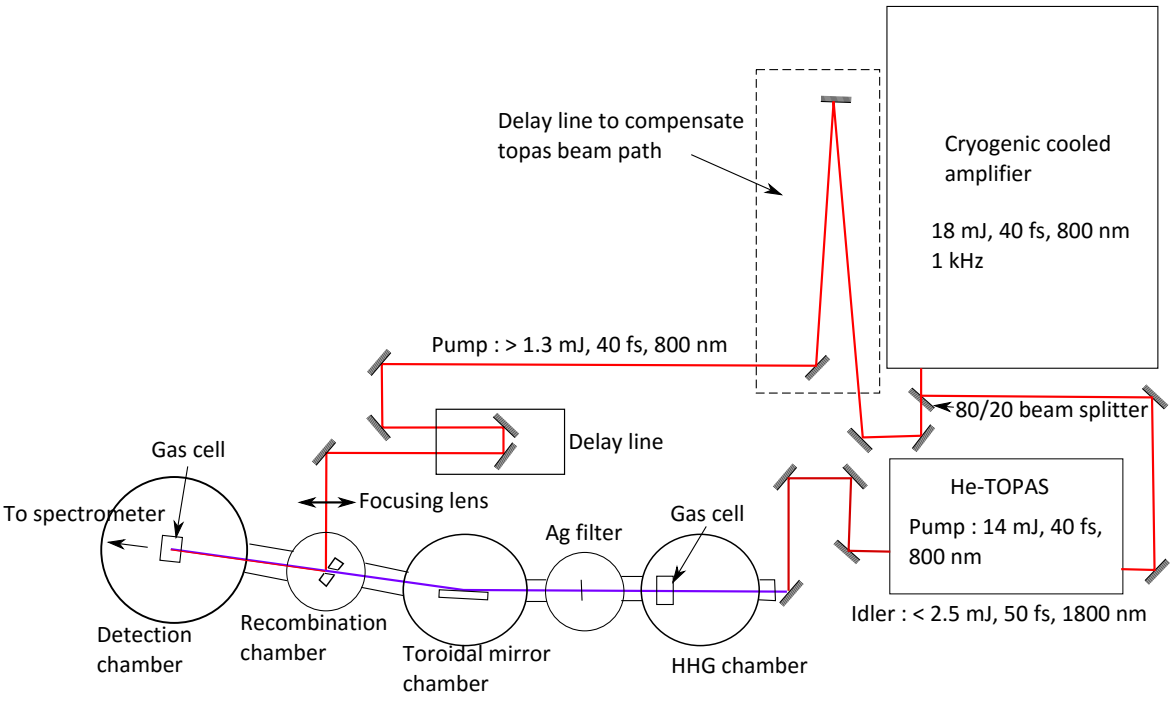

Figure S1: **Experimental setup for soft X-ray transient absorption with a high-harmonic source.** A cryogenically-cooled Ti:Sa laser-amplifier system is used to pump a high-energy optical-parametric amplifier in order to generate multi-mJ pulses centered at 1800 nm used for high-harmonic generation in a gas cell.

The experimental setup is based on a cryogenically-cooled Ti:Sa laser system which delivers up to 18 mJ pulses at 1 kHz repetition rate with 40 fs pulse duration. This intense beam is first split by an 80:20 beam splitter where the most intense part is used for pumping a HE-TOPAS (High-Energy Travelling-wave Optical Parametric Amplifier System) from Light Conversion. About 14 mJ at 800 nm wavelength is converted in the white-light TOPAS in order to obtain up to 2.5 mJ at 1800 nm wavelength in the idler. The 1440 nm signal is separated from the idler by five 1800 nm high-reflection mirrors having extremely low reflectivity at 1440 nm. The 1800 nm pulse was then focused with a f=40 cm CaF_2 lens to generate high harmonics in a static-pressure gas cell filled with neon at 700 mbar pressure and 6 mm length. Both parameters were optimized for maximal flux. The generated soft X-ray beam was then separated from the co-propagating IR with a 100 nm thick silver filter and refocused into a second gas cell containing

the sample gas by means of a nickel-coated toroidal mirror.

The gas targets for high-harmonic generation and transient-absorption measurements were identical. They consisted of a 6 mm inner-diameter tube with two holes drilled by the laser beams themselves. The tubes were placed inside a differentially-pumped cube, itself located within the vacuum chambers. A backing pressure of 700 mbar neon was applied to the HHG target, resulting in a pressure of 1×10^{-2} mbar in the outer vacuum chamber. Under these conditions, filamentation of the driving laser beam was observed as shown in Fig. S2. Backing pressures of 150 mbar CF_4 or 20 mbar SF_6 were applied to the transient-absorption target, resulting in background pressures in the low range of 1×10^{-4} mbar in the outer vacuum chambers, pumped by a 2000 L/s turbomolecular pump.

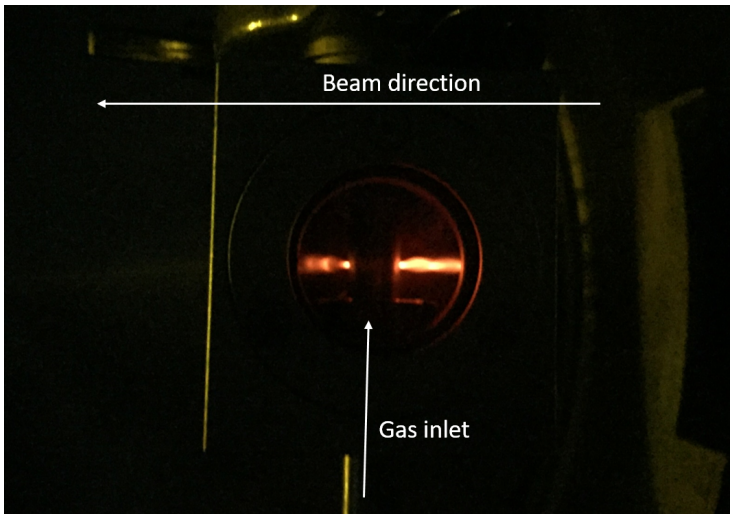

Figure S2: **Picture of the differentially-pumped high-harmonic-generation target.** The pressure gradient of neon in the differentially-pumped region allows for filamentation of the intense mid-IR pulse.

As shown in Fig. S1, 20 percent of the 800 nm power is used for strong-field ionization of the sample gas (CF_4 or SF_6 in the present study). An average pulse energy of about 1.3 mJ on target has been used for most of the scans. A 0.1-micron-precision translation stage allowed us to scan the delay between pump (800 nm, 1.3 mJ, 40 fs) and probe (soft X-rays from high-harmonic generation). A shutter was incorporated into the pump line enabling the measurement of the pumped and unpumped absorption spectra at each delay step. Reference spectra without gas sample were additionally recorded before and after each scan in order to verify the stability

of the laser sources and target pressures. Since the time scale for a scan was about 45 minutes to one hour, only small drifts were observed. However, when reference spectra before and after the scan were different, the data were discarded.

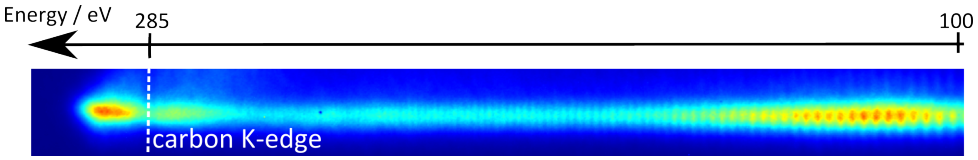

Figure S3: **Experimental raw image of a high-harmonic spectrum generated in neon and recorded with a flat-field imaging spectrometer.** The weak absorption at 285 eV originates from a slight contamination of the toroidal mirror with carbon-containing material. This contamination was removed regularly by treatments of the mirror with ozone.

Absorption spectra were recorded by means of a home-built soft X-ray spectrometer consisting of a variable-size entrance slit, an aberration-corrected flat-field grating (Shimadzu 2400 lines/mm) and a micro-channel plate coupled to a phosphor screen. Images were recorded by a CCD camera (PCO pixelfly USB). An example of a recorded image with an integration time of about five seconds is shown Fig. S3. An experimental resolution of $E/\Delta E = 308$ has been determined by comparing measured absorption spectra of SF_6 with high-resolution measurements from the literature (24). These same spectra, i.e. the positions of the dominant 4 absorption lines of SF_6 (a_{1g}, t_{2g}, e_g bands at the $L_{2,3}$-edge and the t_{1u} band at the L_1-edge) and the position of the carbon K-edge from the carbon-containing contamination on the soft X-ray optics, were used for energy calibration of the spectrometer using the grating equation provided by the manufacturer.

The determination of zero time delay has been done with the following method. After the recombination mirror, a movable "pick-up" mirror allows us to send the beam outside the chamber. The 800-nm and 1800-nm laser pulses are then focused into a fused-silica plate (500 μm thick microscope slides). The intense 800-nm pulse transiently changes the refractive index of the thin fused silica plate, introducing a local increase of transmission of the 1800-nm pulse. The zero-delay position found with this method has been cross-checked by removing the glass and repeating the same experiment in air. Both methods lead to the same result. The delay introduced by the different group velocities of the 1800-nm and the 800-nm pulses as they propagate through the 1 mm magnesium fluoride window at the exit of the vacuum system has

been taken into account. The zero time delay determined in this way will also apply to the 800-nm and soft-X-ray pulses provided that the maxima of the envelopes of the 1800-nm and soft-X-ray pulses coincide. This is the case because the neon target used for high-harmonic generation is only weakly ionized by the 1800-nm pulse ($<$10% at the highest applied intensity of 5×10^{14}W/cm^2 according to ADK calculations including a correction for barrier suppression).

Text S2 **Data analysis**

2.1 Background subtraction and normalization

We first discuss our procedure for experimental data analysis. The relevant quantity in a transient-absorption experiment is the absorbance A defined by:

$$A = \ln\left(\frac{I_0}{I}\right), \tag{1}$$

where I_0 is the spectral intensity of the probe pulse, i.e., the spectrum recorded without gas sample and I is the spectrum after transmission through the sample. Moreover, when the sample is only partially ionized, a reference spectrum I_{ref} of the non-ionized gas sample is required at each delay step. Finally, the plotted quantity can be written as:

$$A = \ln\left(\frac{I_0}{I}\right) - \alpha \ln\left(\frac{I_0}{I_{ref}}\right), \tag{2}$$

where α is a real number between 0 and 1 describing the non-ionized fraction of the probed sample. The necessity to subtract a non-ionized fraction can have two reasons. First, in the interaction volume of the gas sample and the pump beam, a certain fraction of the molecules remains neutral. Second, the ionized and probed volumes may not overlap perfectly. Indeed, the 800 nm pump beam has been focused with a 40 cm focal length, leading to a focal spot size of approximately 100 μm. The 1800 nm beam used for HHG has a similar focusing geometry but a longer wavelength, which leads to a probed volume that is larger than the excited volume. The fraction α is then estimated by comparison between calculated and observed absorption spectra. It has a value of 0.5$\pm$0.1 in the CF_4 data set and 0.55$\pm$0.1 in the SF_6 measurements, which was determined by iterative adjustment in the data sets shown in Figs. 2 and 4 of the main text.

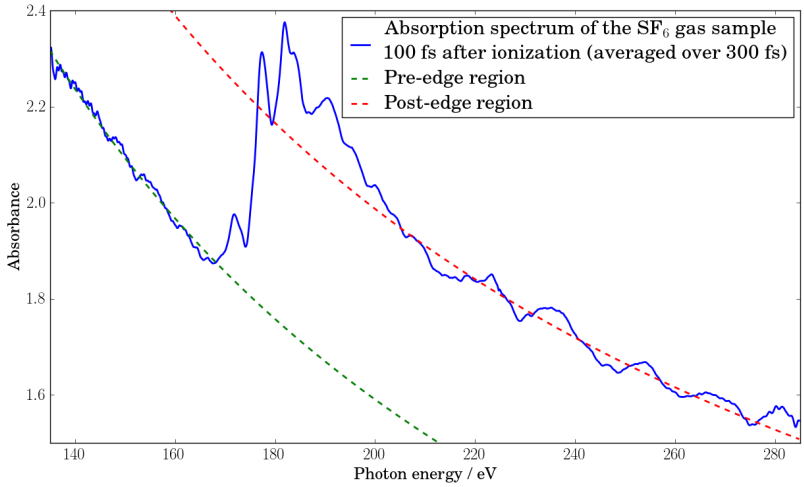

Figure S4: **Illustration of the background correction in a typical sulfur L-edge absorption spectrum** Absorption spectrum averaged over time delays from 100 to 400 fs during the dissociation of SF_6^+. The pre-edge and post-edge regions have been fitted using the Larch X-ray python library.

A typical near-edge absorption spectrum of SF_6 following strong-field ionization and subsequent dissociation is shown in Fig. S4. The spectra measured in our SF_6 experiments cover both the XANES (X-ray absorption near-edge structure) and EXAFS (extended X-ray absorption fine structure) regions. The common procedure for the analysis of such X-ray absorption spectra consists of two steps. First, polynomial fitting of the background absorption, followed by its subtraction in the pre-edge region (green line in Fig. S4), and second, normalization with a polynomial fit to the post-edge tail (red line in Fig. S4). In the present work, we have focused on the XANES part of the spectra and have therefore only applied the pre-edge background correction. The second part, i.e. normalization of the post-edge region is only important for an EXAFS analysis, which was not possible in the present study because of strong L_1 absorption features in SF_6 and a lack of spectral coverage in CF_4.

In the particular case of the L_1-edge of SF_6, a constant linear background has been fitted and subtracted from the entire L_1 region without more detailed consideration of pre- or post-edges. In this case, the main contribution to the pre-edge background corresponds to the slowly decreasing absorption tail from the $L_{2,3}$-edges of SF_6.

2.2 Carbon K-edge transient absorption of CF_4

The data shown in Fig. 2B of the main text is shown as a two-dimensional version in Fig. S5. The dissociation time and the time resolution have been determined by selecting 6 different 0.5-eV-wide energy ranges from 285 eV to 288 eV, corresponding to the appearance of the $2a_2''$ absorption band assigned to CF_3^+. A step function convoluted with a Gaussian has been fitted to each of these signal. Since a very narrow energy band has been selected for this analysis, one can assume that the time broadening is dominated by the experimental time resolution. The individual results are averaged. In this way, we obtain an a time resolution of (40±5) fs. The center of the error function, which represents the delayed appearance the $2a_2''$ absorption band of CF_3^+ is a measure of the dissociation time of the reaction $CF_4^+ \rightarrow CF_3^+ + F$. We find that the appearance of CF_3^+ is delayed by (40±2) fs (see Table S1), suggesting a very fast dissociation reaction, in agreement with the steeply repulsive reaction-path potential curve shown in Fig. S7.

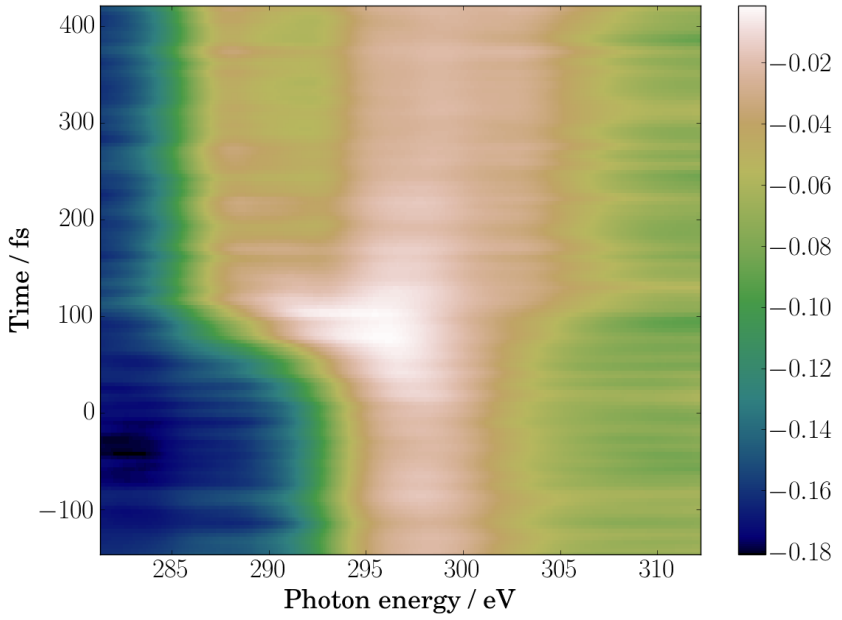

Figure S5: **Soft-X-ray transient-absorption spectra of the dissociation of CF_4^+.** This is a two-dimensional representation of the same data as in Fig. 2B of the main text.

CF_4^+	Δt (fs)	error = $\frac{\sigma}{\sqrt{n}}$ (fs)
a_2''	40	2
SF_6^+		
a_{1g}	34	4
t_{2g} (lower comp.)	74	10
t_{2g} (upper comp.)	40	8
e_g	46	4

Table S1: Table summarizing the time delays for the appearance of characteristic absorption bands of the fragments, obtained by fitting an error function to the intensity of the asymptotic absorption bands. In the case of CF_4, the $2a_2''$ absorption band of CF_3^+ was analyzed. In the case of SF_6, the labels refer to the absorption bands of SF_6 that correlate with the analyzed absorption bands of SF_5^+ in order of increasing energy. The errors are purely statistical and do not include the additional error in the determination of $t = 0$, which is estimated to $\pm$15 fs.

2.3 Sulfur L-edges transient absorption of SF_6

The data treatment in the case of SF_6 was very similar to that of CF_4. The data from Figs. 4B and 4C of the main text is shown as a two-dimensional representation in Fig. S6. As in the case of CF_4, a fit of a step function convoluted by a Gaussian has been made to four selected regions of the spectrum, corresponding to the dominant absorption features of SF_5^+. The following energy ranges were chosen: 168.5-169 eV (corresponding to the a_{1g} absorption band in SF_6 correlating with the a_1' band in SF_5^+), 175.9-176.5 eV (t_{2g} in SF_6 correlating with the lower-lying absorption band in SF_5^+), 180.6-181.2 eV (t_{2g} in SF_6 correlating with the higher-lying absorption band in SF_5^+) and 187.6-188.2 eV (e_g in SF_6 correlating with the broad absorption band in SF_5^+)). This analysis additionally determines the time resolution of the experiment to be (45$\pm$7) fs (as an average over the 4 bands).

Each of these four absorption bands yields a slightly different dissociation time (see Table S1), ranging from (34$\pm$4) fs to (74$\pm$10) fs. These time scales again suggest a very fast dissociation reaction. We interpret the differences in the appearance times of these four absorption bands as reflecting the different sensitivities of the final states of the X-ray transitions to the dissociation reaction of SF_6^+.

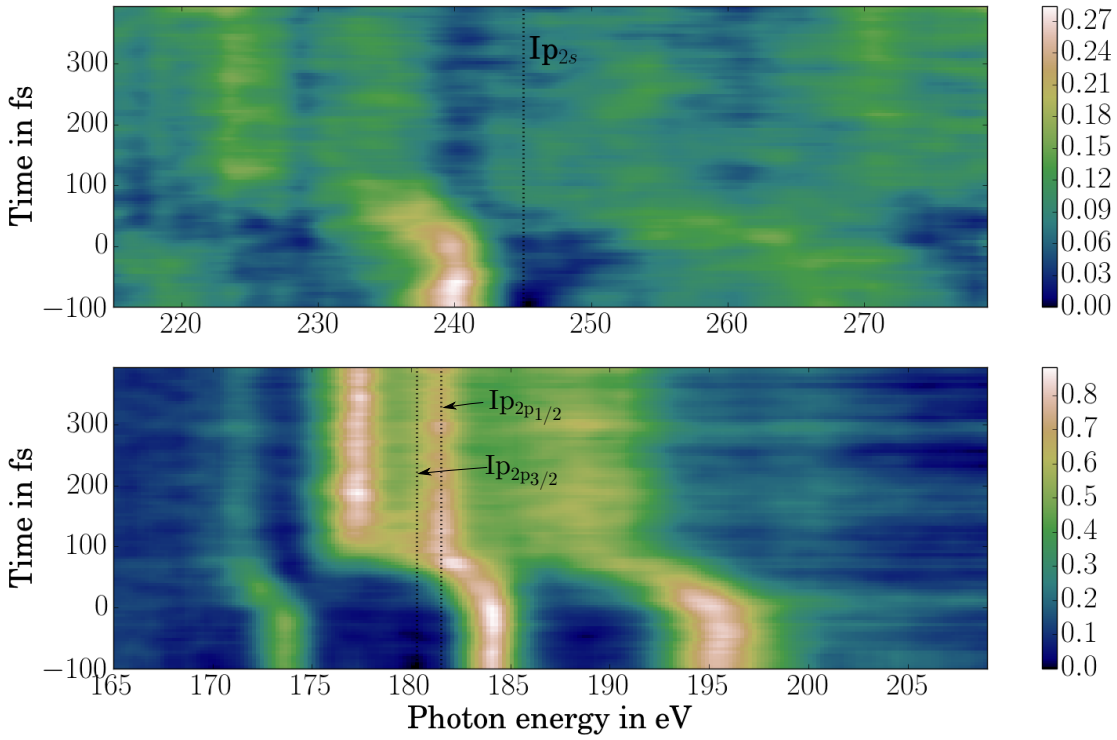

Figure S6: **Soft-X-ray transient absorption spectra of the dissociation of SF_6^+.** The upper panel shows the time-dependent absorption spectra at the sulfur L_1-edge, whereas the lower panel shows the sulfur $L_{2,3}$-edge region. The dashed line shows the sulfur-L-edge ionization thresholds of neutral SF_6.

Text S3 Ab-initio quantum chemical calculations of CF_4

The numerical calculations presented in Fig. 3 of the main text were obtained in two steps.

3.1 Minimum-energy reaction-path calculations of CF_4

First, the minimum-energy reaction path for the reaction

$$CF_4^+ \rightarrow CF_3^+ + F \tag{3}$$

was calculated using the Gaussian09 package at the coupled-cluster singles-doubles CCSD/6-31G* level of theory. The C-F internuclear separation has been fixed to a range of values between 1.32 and 5.3 Å and all other degrees of freedom have been relaxed in order to minimize the potential energy of the electronic ground state of $[CF_3\text{-}F]^+$ for each point along the

dissociation path.

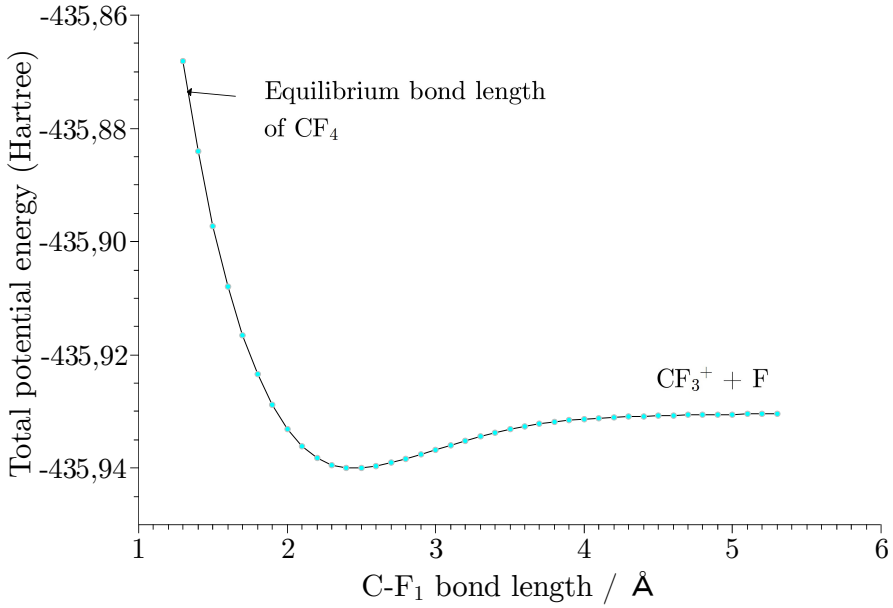

Figure S7: **Potential-energy curve of the minimum-energy reaction path in the electronic ground state of CF_4^+ as a function of one fixed C-F internuclear separation**

Figure S7 shows the potential-energy curve as a function of the C-F internuclear separation for the electronic ground state of CF_4^+. It exhibits a minimum at a bond length of 2.5 Å which corresponds to a geometry of C_{3v} symmetry. The 0.25 eV depth of this minimum is smaller than the zero-point vibrational energy of CF_4^+ (27) and much smaller than the internal energy of CF_4^+ following strong-field ionization from the equilibrium geometry of CF_4 in its electronic ground state, which is indicated in Fig. S7. Consequently, all CF_4^+ molecules created by strong-field ionization are expected to dissociate, which is consistent with our experimental observations.

Our calculations have only addressed the electronic ground state of CF_4^+. Our conclusions are consistent with the experimental literature on this molecule, i.e. the absence of CF_4^+ from mass spectra. Although we have not calculated the potential-energy surfaces for the electronically-excited states of the cation, it has been shown that CF_4^+ also dissociates by loosing one fluorine atom in their first and second electronically-excited states (26). A more advanced theoretical treatment would require the calculation of at least the three lowest potential-energy surfaces in full dimensionality (9 dimensions in the case of CF_4^+) and wave-packet propagation on these coupled surfaces. This is out of reach for state-of-the-art theoretical methods.

3.2 Calculations of X-ray absorption spectra of CF_4

The second part of the calculations consists in calculating the near-edge X-ray absorption spectra for each of the different geometries calculated along the mininum-energy reaction path using time-dependent density-functional theory (TDDFT). We will now describe in more detail the TDDFT calculations that we have performed and discuss the different methods employed and their possible influence on the outcome of the calculation. The following calculations have been performed with the ADF suite of programs.

A Slater-type basis set of quadruple-zeta quality augmented with 4 polarization functions has been used for all the atoms of CF_4. Further improvement of this (very good) basis set made the calculations of X-ray absorption spectra for the required 60 different geometries intractable (using the Euler high-performance cluster at ETH Zürich). The present basis set has consequently been identified to yield the best possible accuracy with a manageable computational effort. These calculations were done within the electric-dipole approximation and did not include shake-down processes. Because these calculations do not include spectral broadening originating from lifetime effects and final-state vibrational structure, each absorption band appears as a sharp peak, in contrast to the experiment, where both effects contribute to the broadening of the bands.

We performed unrestricted TDDFT calculations for each geometry along the minimum-energy reaction path because of the open-shell nature of CF_4^+. Such calculations can only be done without symmetry in ADF. In order to assign the electronic symmetries, in particular at the end of the reaction, a restricted calculation on the closed-shell molecule CF_3^+ has been done and compared to the open shell CF_3^+-F system at very long C-F internuclear separations. The calculated absorption spectra were extremely similar, such that all the orbital symmetries of the final product were easily obtained by comparison. Another important parameter of the calculation is the choice of the exchange-correlation functional. In the present work, we have used the LB94 functional. This functional is particularly suitable for describing the asymptotic behavior of the electron-ion potential, which is important to achieve accurate results close to the ionization threshold and for ionic species. Finally, all the calculated absorption spectra were plotted together as a function of one C-F internuclear separation. The result is shown in Fig.

3A of the manuscript. The internuclear separations only range from 1.32 to 2.56 Å, because the calculated spectra for C-F internuclear separations longer than 2.5 Å are all identical.

Text S4 **Reconstruction of the time-dependent C-F internuclear separation**

4.1 Extraction of the $2a_2''$ absorption band from experimental data

As shown in Fig. 3 of the main text, one of the main experimental features that is well represented in the TDDFT calculations is the splitting of the $5t_2$ absorption band of CF_4 and the very large shift of the $2a_2''$ band during the dissociation of CF_4^+ to CF_3^+. The first step in the reconstruction of the CF_3^+-F separation as a function of time is the determination of the position of this absorption band at each delay. This has been achieved by fitting the background absorption in CF_4 (i.e. the absorption at $t < 0$, see Fig. S8) and subtracting this background from the entire scan. This data-analysis approach combined with the application of a rectangular energy filter with a width of 12 eV enables the isolation of a single absorption band and its accurate analysis as shown in Fig. S9.

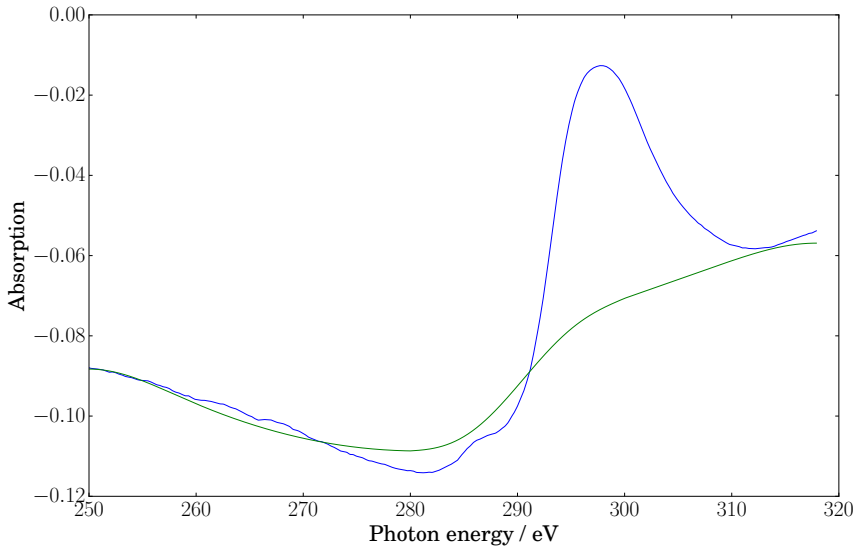

Figure S8: **Fit to the background absorption of CF_4.** The fit to the background absorption of CF_4 (using spectra recorded at $t < 0$) is subtracted from the whole data set in order to isolate the lowest absorption band, corresponding to the C 1s→$2a_2''$ transition.

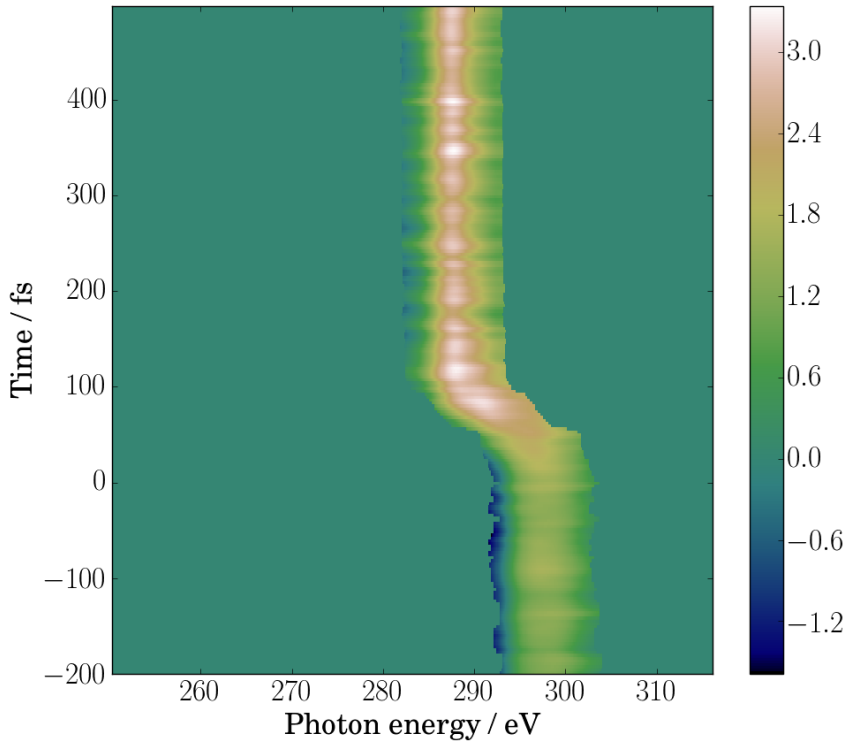

Figure S9: **Position of the $5t_2$ / $2a_2''$ absorption band extracted from the experimental data.** The strong shift in energy of the $2a_2''$ absorption band originating from the $5t_2$ band in CF_4 as extracted from experimental absorption data.

Next, the position of the absorption maximum was determined at each delay. Two methods have been used and compared in order to test the robustness of the present analysis. The first method consisted in extracting the center of mass of the absorption band whereas the second one was a fit of the extracted absorption band by a Gaussian function at each time delay. Several parameters have been tested (box size, initial parameters of the peak-finding algorithm) and a convergence of both methods to very similar results has been observed. Moreover, several types of background corrections have been compared and all of them gave very similar results. The final result on the delay-dependent position of the absorption maximum is shown in Fig. S10.

4.2 Reconstruction of the C-F internuclear separation from experimental data

The time-dependent position of the absorption maximum, obtained from the method described in the previous section is then compared to the calculated position as a function of the C-F internuclear separation from our CCSD/6-31G* reaction path calculations. Owing to the limited accuracy of the TDDFT calculations, observed and calculated positions of the relevant absorption bands do not agree quantitatively (cp. Figs. 2B and 3A in the main text). Prior to performing the reconstruction, we therefore applied a linear scaling of the energy axis to match the positions of the dominant absorption bands in both CF_4 and CF_3^+. This approach corrects the inaccuracies of the TDDFT calculations in reproducing the absolute energy of the X-ray transition, while simultaneously preserving the time-resolved information contained in the measurements.

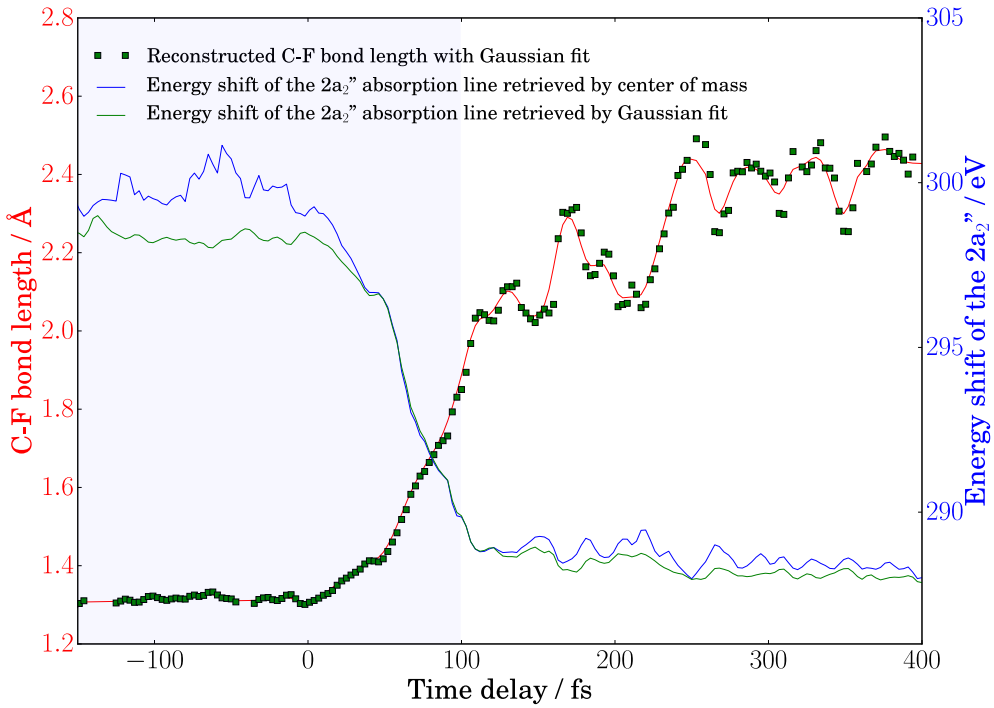

Figure S10: **Reconstructed C-F internuclear separation as a function of the time delay between pump and probe pulses.** We consider the validity of this reconstruction to be limited to delays below ∼100 fs (blue-shaded area). The oscillations observed a longer delays are attributed to vibrational dynamics of CF_3^+.

The observed time-dependent position of the $2a_2''$ absorption band and its calculated position

as a function of the C-F internuclear separation can then be combined to reconstruct the C-F internuclear separation as a function of the time delay between the 800 nm pump pulse and the soft X-ray probe. The results are show Fig. S10. The reconstructed internuclear separation shows the expected acceleration at early time delays that originates from the motion of the nuclear wave packet on the repulsive potential energy surface of CF_4^+ (see Fig. S7). The increase of the internuclear separation then becomes practically linear with time until ∼120 fs. For longer times and C-F distances beyond 2.0 Å, the reconstruction method fails because the absorption band of the CF_3^+-F complex has converged to its position in the isolated CF_3^+ molecule once the electronic overlap with the F atom is sufficiently small. However, Fig. S10 reveals pronounced oscillations of the energy position of the absorption maximum, both during dissociation and at longer delays, that we discuss in the next section.

4.3 Fourier analysis and interpretation

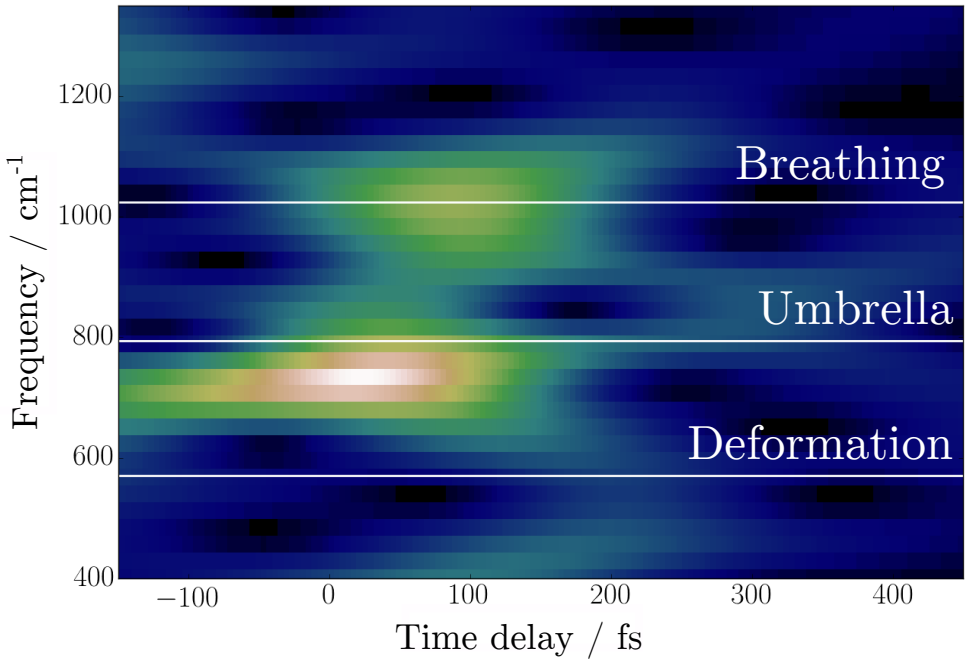

Figure S11: **Sliding-window Fourier transform of the energy shift of the $2a_2''$ absorption band of CF_3^+.** A temporal window with a width of 100 fs has been used. The white lines indicate the vibrational frequencies of CF_3^+.

During and after dissociation, the position of the $2a_2''$ band in energy appears to oscillate. We therefore performed a sliding-window Fourier transformation of these data, which is shown in Fig. S11. The white lines correspond to the wavenumbers of the vibrational modes of the CF_3^+ cation in its electronic ground state with D_{3h} symmetry. The values were taken from a spectroscopic measurement on isolated molecules in the gas phase (36). These results suggest that the umbrella mode of CF_3^+ is transiently excited during the dissociation, followed by excitation of the breathing mode. The primary excitation of the umbrella mode is consistent with the fact that the molecular geometry changes from tetrahedral at early delays to trigonal planar at longer delays. The limited frequency resolution in these data do however not allow us to draw more quantitative conclusions.

Text S5 Interpretation of the dissociative ionization of SF_6

5.1 Experimental observations

5.1.1 Quantitative analysis of the absorption bands

Using the same method as in the case of CF_4^+, we show in Fig. S12 the positions of four dominant absorption bands identified in the time-resolved absorption spectra of SF_6^+. These positions have been determined at each delay from the center of mass of the absorption in these four regions. Figure S13 shows a renormalized version of the energy shift of these absorption bands. In this figure, very small delays between the dynamics of the individual absorption bands are observed. These small delays are consistent with the delays reported in Table S1 that describe the appearance time of the fragment (SF_5^+) absorption bands. Indeed, the a_{1g} is the first band to shift in energy, followed by the higher-lying component of the t_{2g} line, and the e_g line is the last to shift. The splitting of the t_{2g} resonance is delayed with respect to the onset of the energy shifts of the other two bands by $\sim$70 fs. We propose an explanation of this observation in Section 5.2.

According to our calculations, the global shift of all absorption bands to lower energies is dominated by a core-level shift of the sulfur atom. The loss of one electronegative fluorine atom during the dissociation causes the core orbital to shift to smaller (less negative) binding energies, lowering the photon energy of the absorbing transition.

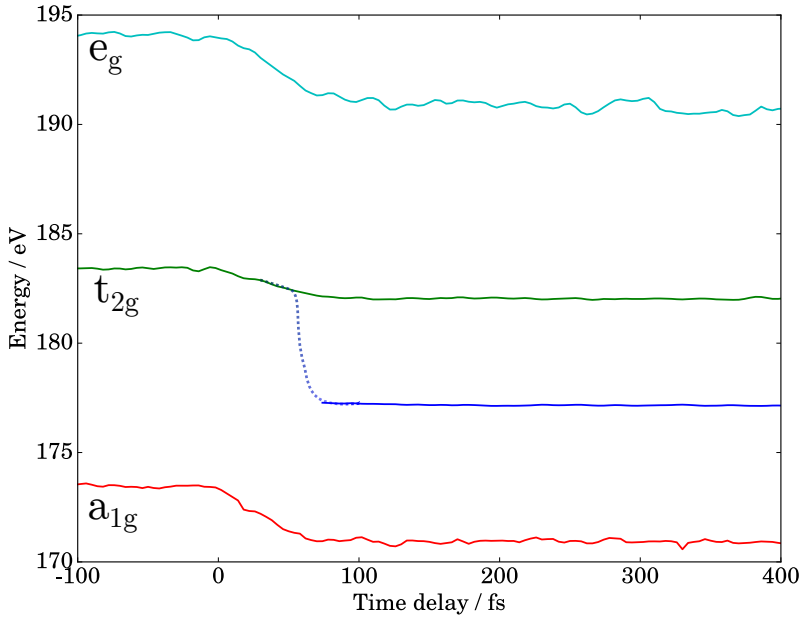

Figure S12: **Observed shift of the absorption bands observed during the dissociation of SF_6^+.** Observed center of mass of the absorption bands during the dissociation of SF_6^+ to SF_5^+ + F. The dotted line is a guide to the eye and was not extracted from experimental data.

5.1.2 Intensity dependence of the observed dynamics

Figure S14 shows the effect of the pump intensity on the transient-absorption spectra of SF_6. Whereas Fig. S6 and Fig. 4 of the main text show data recorded using a pump-pulse intensity (upper limit) of $\sim 5 \times 10^{14}$ W/cm^2, Fig. S14A and S14B show data recorded at $\sim 3 \times 10^{14}$ W/cm^2 and $\sim 7 \times 10^{14}$ W/cm^2, respectively. The comparison of Figs. S6, S14A and S14B reveals no noticeable dependence of the observed dynamics on the intensity. We therefore conclude that the observed dynamics can entirely be attributed to the main dissociation channel $SF_6^+ \rightarrow SF_5^+ + F$ and that the contributions of dissociation channels of doubly-charged SF_6^{2+} are negligible in our observations.

5.2 Theoretical analysis and interpretation

We performed the same calculations as in the case of CF_4 in order to obtain the potential-energy curve of the reaction path $SF_6^+ \longrightarrow SF_5^+ + F$. The results are shown in Fig. S15. We performed TDDFT calculations of the absorption spectra for each geometry along the reaction path. The

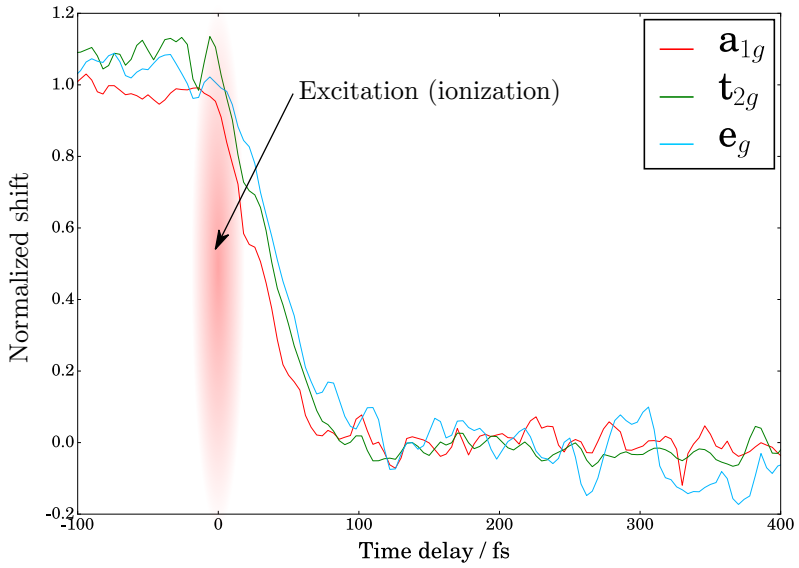

Figure S13: **Normalized shift of the observed absorption bands during the dissociation of SF_6^+.** Time-dependent energy shifts after normalization of the initial and final energies to one and zero, respectively. The red feature illustrates the time interval over which strong-field ionization takes place.

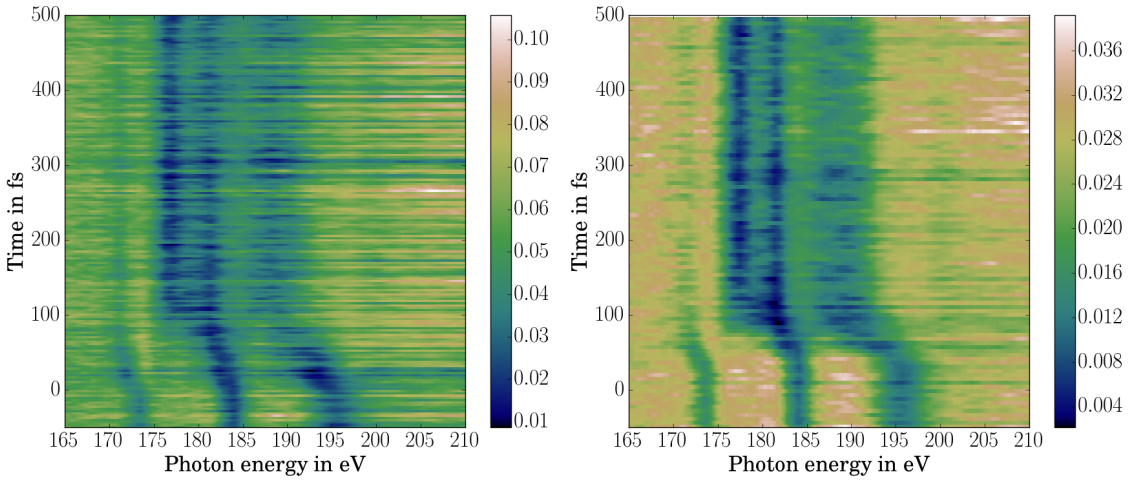

Figure S14: **Time-dependent absorption spectra of dissociating SF_6^+ at two different intensities.** (left) Time-dependent absorption spectra as a function of the time delay between pump and probe pulses at low pump intensity ($\sim 3 \times 10^{14}$ W/cm^2). (right) time-dependent spectra at high pump intensity ($\sim 7 \times 10^{14}$ W/cm^2).

results are presented in Fig. S16.

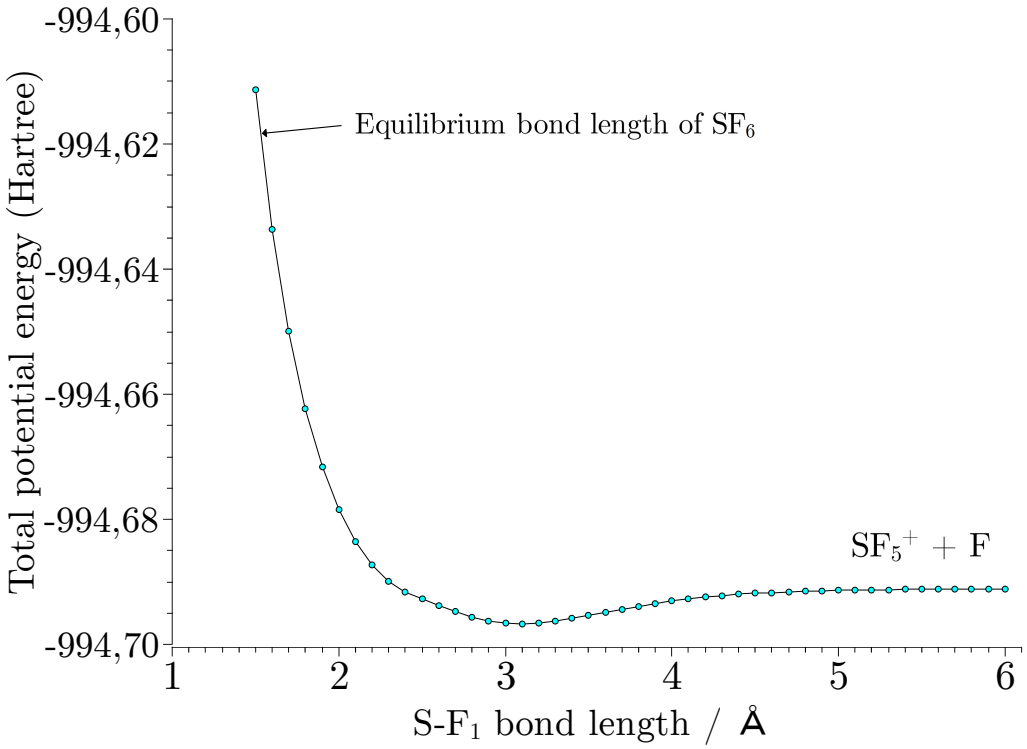

Figure S15: **Potential-energy curve of the minimum-energy reaction path in the electronic ground state of SF_6^+ as a function of one S-F internuclear separation.**

Turning to the interpretation, we first discuss experimental and calculated results on the evolution of the a_{1g} and e_g absorption bands of SF_6. The most noticeable feature is a shift of both absorption bands to lower photon energies, the $6a_{1g}$ band correlating with the $9a_1'$ band in SF_5^+. The $7e_g$ resonance broadens very rapidly as a function of the S-F bond length through the appearance of additional resonances on both sides, which partially merge to produce a broad absorption band consisting of multiple shape resonances in SF_5^+. The $3t_{2g}$ absorption band is also correctly predicted to split into two dominant absorption bands, and this splitting is predicted to occur at much longer S-F bond lengths than the shift of the $6a_{1g}$ and $7e_g$ bands. Both predictions agree with the experimental observations. However, the two bands resulting from this splitting are found to shift to lower photon energies in the experimental data (Fig. 4B and S6), whereas the calculation predicts one band to shift to higher energies. This discrepancy between experiment and theory is attributed to the limited accuracy of the TDDFT calculation

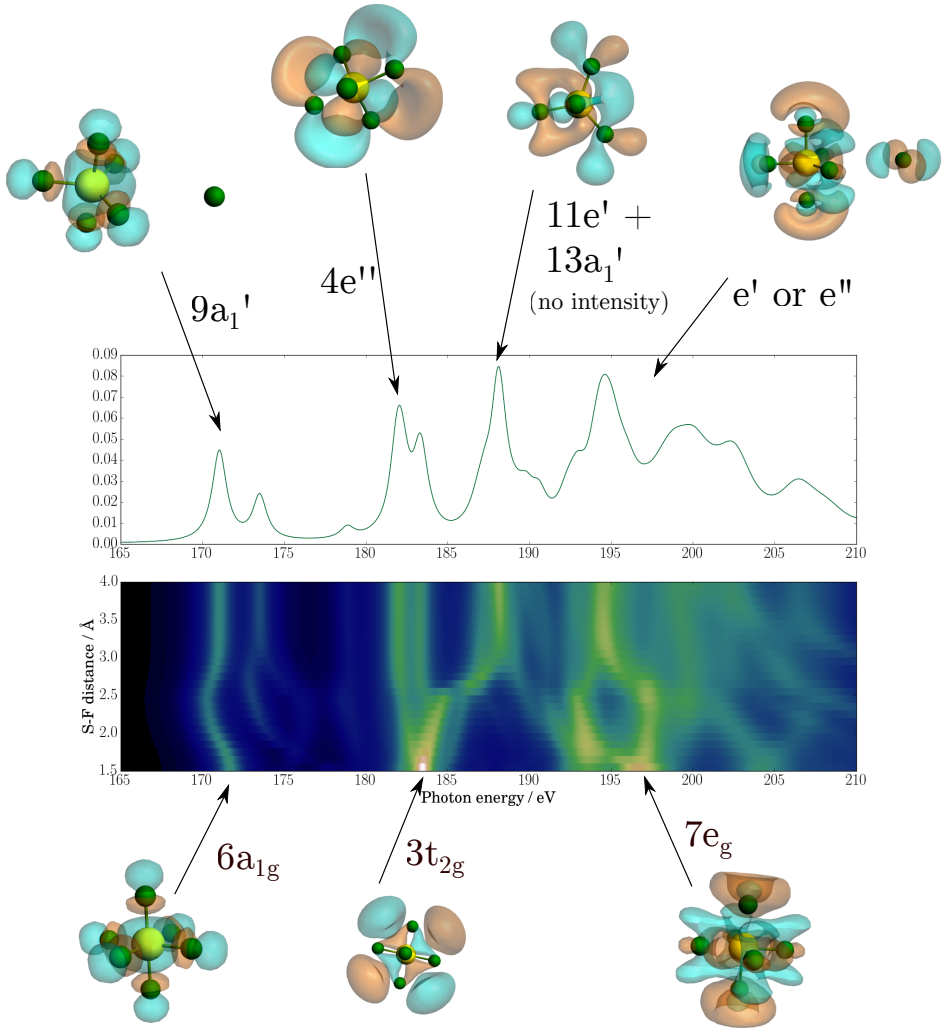

Figure S16: **Calculated absorption spectra along the dissociative reaction path of SF_6^+.** The calculated absorption spectrum of SF_5^+ is shown above the two-dimensional spectrogram. Labelling of the dominant absorption bands and shape of the orbitals is shown in order to illustrate the transformations taking place.

of the X-ray absorption spectra in reproducing energy shifts on a quantitative level. A similar, but less dramatic discrepancy has been pointed out in the case of the CF_4^+ dissociation.

Why does the splitting of the t_{2g} band start at a much longer internuclear separation than the shift of the a_{1g} and e_g bands? This is attributed to a rapid change of the FSF bond angles occurring in the range of S-F bond distances from 2.5 to 3 Å. This rapid change of the bond angles causes a strong variation of the energy of the unoccupied final states responsible for the dominant absorption features close to the sulfur $L_{2,3}$-edge (the $3t_{2g}$ orbital in SF_6 and the $11e'$

orbital in SF_5^+). These orbitals are shown in Fig. S16, together with the other relevant orbitals of SF_6 (bottom) and SF_5^+ (top). Whereas the $3t_{2g}/11e'$ orbitals have the largest amplitudes in the space between the fluorine atoms, the $6a_{1g}/9a_1'$ and $7e_g$/correlating e-type orbitals have no amplitude or nodal planes in between the fluorine atoms. These differences in the structure of the orbitals is consistent with the different response of the corresponding absorption bands to the bond-angle change. We therefore propose that the observed delay in splitting of the t_{2g} band originates from the different spatial structure of the associated one-electron orbitals describing the t_{2g} shape resonance in SF_6. More accurate calculations will be required to further verify this conclusion.

References

1. M. H. F. Wilkins, A. R. Stokes, H. R. Wilson, Molecular structure of deoxypentose nucleic acids. *Nature* **171**, 738–740 (1953). doi:10.1038/171738a0 Medline

2. J. A. van Bokhoven, C. Lamberti, Eds., *X-Ray Absorption and X-Ray Emission Spectroscopy: Theory and Applications* (Wiley, 2016).

3. Ch. Bressler, C. Milne, V.-T. Pham, A. Elnahhas, R. M. van der Veen, W. Gawelda, S. Johnson, P. Beaud, D. Grolimund, M. Kaiser, C. N. Borca, G. Ingold, R. Abela, M. Chergui, Femtosecond XANES study of the light-induced spin crossover dynamics in an iron(II) complex. *Science* **323**, 489–492 (2009). doi:10.1126/science.1165733 Medline

4. W. Ackermann, G. Asova, V. Ayvazyan, A. Azima, N. Baboi, J. Bähr, V. Balandin, B. Beutner, A. Brandt, A. Bolzmann, R. Brinkmann, O. I. Brovko, M. Castellano, P. Castro, L. Catani, E. Chiadroni, S. Choroba, A. Cianchi, J. T. Costello, D. Cubaynes, J. Dardis, W. Decking, H. Delsim-Hashemi, A. Delserieys, G. Di Pirro, M. Dohlus, S. Düsterer, A. Eckhardt, H. T. Edwards, B. Faatz, J. Feldhaus, K. Flöttmann, J. Frisch, L. Fröhlich, T. Garvey, U. Gensch, C. Gerth, M. Görler, N. Golubeva, H.-J. Grabosch, M. Grecki, O. Grimm, K. Hacker, U. Hahn, J. H. Han, K. Honkavaara, T. Hott, M. Hüning, Y. Ivanisenko, E. Jaeschke, W. Jalmuzna, T. Jezynski, R. Kammering, V. Katalev, K. Kavanagh, E. T. Kennedy, S. Khodyachykh, K. Klose, V. Kocharyan, M. Körfer, M. Kollewe, W. Koprek, S. Korepanov, D. Kostin, M. Krassilnikov, G. Kube, M. Kuhlmann, C. L. S. Lewis, L. Lilje, T. Limberg, D. Lipka, F. Löhl, H. Luna, M. Luong, M. Martins, M. Meyer, P. Michelato, V. Miltchev, W. D. Möller, L. Monaco, W. F. O. Müller, O. Napieralski, O. Napoly, P. Nicolosi, D. Nölle, T. Nuñez, A. Oppelt, C. Pagani, R. Paparella, N. Pchalek, J. Pedregosa-Gutierrez, B. Petersen, B. Petrosyan, G. Petrosyan, L. Petrosyan, J. Pflüger, E. Plönjes, L. Poletto, K. Pozniak, E. Prat, D. Proch, P. Pucyk, P. Radcliffe, H. Redlin, K. Rehlich, M. Richter, M. Roehrs, J. Roensch, R. Romaniuk, M. Ross, J. Rossbach, V. Rybnikov, M. Sachwitz, E. L. Saldin, W. Sandner, H. Schlarb, B. Schmidt, M. Schmitz, P. Schmüser, J. R. Schneider, E. A. Schneidmiller, S. Schnepp, S. Schreiber, M. Seidel, D. Sertore, A. V. Shabunov, C. Simon, S. Simrock, E. Sombrowski, A. A. Sorokin, P. Spanknebel, R. Spesyvtsev, L. Staykov, B. Steffen, F. Stephan, F. Stulle, H. Thom, K. Tiedtke, M. Tischer, S. Toleikis, R. Treusch, D. Trines, I. Tsakov, E. Vogel, T. Weiland, H. Weise, M. Wellhöfer, M. Wendt, I. Will, A. Winter, K. Wittenburg, W. Wurth, P. Yeates, M. V. Yurkov, I. Zagorodnov, K. Zapfe, Operation of a free-electron laser from the extreme ultraviolet to the water window. *Nat. Photonics* **1**, 336–342 (2007). doi:10.1038/nphoton.2007.76

5. P. Emma, R. Akre, J. Arthur, R. Bionta, C. Bostedt, J. Bozek, A. Brachmann, P. Bucksbaum, R. Coffee, F.-J. Decker, Y. Ding, D. Dowell, S. Edstrom, A. Fisher, J. Frisch, S. Gilevich, J. Hastings, G. Hays, P. Hering, Z. Huang, R. Iverson, H. Loos, M. Messerschmidt, A. Miahnahri, S. Moeller, H.-D. Nuhn, G. Pile, D. Ratner, J. Rzepiela, D. Schultz, T. Smith, P.

Stefan, H. Tompkins, J. Turner, J. Welch, W. White, J. Wu, G. Yocky, J. Galayda, First lasing and operation of an ångstrom-wavelength free-electron laser. *Nat. Photonics* **4**, 641–647 (2010). doi:10.1038/nphoton.2010.176

6. T. Ishikawa, H. Aoyagi, T. Asaka, Y. Asano, N. Azumi, T. Bizen, H. Ego, K. Fukami, T. Fukui, Y. Furukawa, S. Goto, H. Hanaki, T. Hara, T. Hasegawa, T. Hatsui, A. Higashiya, T. Hirono, N. Hosoda, M. Ishii, T. Inagaki, Y. Inubushi, T. Itoga, Y. Joti, M. Kago, T. Kameshima, H. Kimura, Y. Kirihara, A. Kiyomichi, T. Kobayashi, C. Kondo, T. Kudo, H. Maesaka, X. M. Maréchal, T. Masuda, S. Matsubara, T. Matsumoto, T. Matsushita, S. Matsui, M. Nagasono, N. Nariyama, H. Ohashi, T. Ohata, T. Ohshima, S. Ono, Y. Otake, C. Saji, T. Sakurai, T. Sato, K. Sawada, T. Seike, K. Shirasawa, T. Sugimoto, S. Suzuki, S. Takahashi, H. Takebe, K. Takeshita, K. Tamasaku, H. Tanaka, R. Tanaka, T. Tanaka, T. Togashi, K. Togawa, A. Tokuhisa, H. Tomizawa, K. Tono, S. Wu, M. Yabashi, M. Yamaga, A. Yamashita, K. Yanagida, C. Zhang, T. Shintake, H. Kitamura, N. Kumagai, A compact X-ray free-electron laser emitting in the sub-ångström region. *Nat. Photonics* **6**, 540–544 (2012). doi:10.1038/nphoton.2012.141

7. E. Allaria, R. Appio, L. Badano, W. A. Barletta, S. Bassanese, S. G. Biedron, A. Borga, E. Busetto, D. Castronovo, P. Cinquegrana, S. Cleva, D. Cocco, M. Cornacchia, P. Craievich, I. Cudin, G. D'Auria, M. Dal Forno, M. B. Danailov, R. De Monte, G. De Ninno, P. Delgiusto, A. Demidovich, S. Di Mitri, B. Diviacco, A. Fabris, R. Fabris, W. Fawley, M. Ferianis, E. Ferrari, S. Ferry, L. Froehlich, P. Furlan, G. Gaio, F. Gelmetti, L. Giannessi, M. Giannini, R. Gobessi, R. Ivanov, E. Karantzoulis, M. Lonza, A. Lutman, B. Mahieu, M. Milloch, S. V. Milton, M. Musardo, I. Nikolov, S. Noe, F. Parmigiani, G. Penco, M. Petronio, L. Pivetta, M. Predonzani, F. Rossi, L. Rumiz, A. Salom, C. Scafuri, C. Serpico, P. Sigalotti, S. Spampinati, C. Spezzani, M. Svandrlik, C. Svetina, S. Tazzari, M. Trovo, R. Umer, A. Vascotto, M. Veronese, R. Visintini, M. Zaccaria, D. Zangrando, M. Zangrando, Highly coherent and stable pulses from the FERMI seeded free-electron laser in the extreme ultraviolet. *Nat. Photonics* **6**, 699–704 (2012). doi:10.1038/nphoton.2012.233

8. F. Ráksi, K. R. Wilson, Z. Jiang, A. Ikhlef, C. Y. Côté, J.-C. Kieffer, Ultrafast x-ray absorption probing of a chemical reaction. *J. Chem. Phys.* **104**, 6066 (1996). doi:10.1063/1.471305

9. M. Bargheer, N. Zhavoronkov, Y. Gritsai, J. C. Woo, D. S. Kim, M. Woerner, T. Elsaesser, Coherent atomic motions in a nanostructure studied by femtosecond X-ray diffraction. *Science* **306**, 1771–1773 (2004). doi:10.1126/science.1104739 Medline

10. Ch. Spielmann, N. H. Burnett, S. Sartania, R. Koppitsch, M. Schnürer, C. Kan, M. Lenzner, P. Wobrauschek, F. Krausz, Generation of coherent X-rays in the water window using 5-femtosecond laser pulses. *Science* **278**, 661–664 (1997). doi:10.1126/science.278.5338.661

11. E. Seres, J. Seres, F. Krausz, C. Spielmann, Generation of coherent soft-X-ray radiation extending far beyond the titanium L edge. *Phys. Rev. Lett.* **92**, 163002 (2004). doi:10.1103/PhysRevLett.92.163002 Medline

12. E. Seres, C. Spielmann, Ultrafast soft x-ray absorption spectroscopy with sub-20-fs resolution. *Appl. Phys. Lett.* **91**, 121919 (2007). doi:10.1063/1.2789732

13. E. J. Takahashi, T. Kanai, K. L. Ishikawa, Y. Nabekawa, K. Midorikawa, Coherent water window x ray by phase-matched high-order harmonic generation in neutral media. *Phys. Rev. Lett.* **101**, 253901 (2008). doi:10.1103/PhysRevLett.101.253901 Medline

14. M.-C. Chen, P. Arpin, T. Popmintchev, M. Gerrity, B. Zhang, M. Seaberg, D. Popmintchev, M. M. Murnane, H. C. Kapteyn, Bright, coherent, ultrafast soft X-ray harmonics spanning the water window from a tabletop light source. *Phys. Rev. Lett.* **105**, 173901 (2010). doi:10.1103/PhysRevLett.105.173901 Medline

15. T. Popmintchev, M.-C. Chen, D. Popmintchev, P. Arpin, S. Brown, S. Alisauskas, G. Andriukaitis, T. Balciunas, O. D. Mücke, A. Pugzlys, A. Baltuska, B. Shim, S. E. Schrauth, A. Gaeta, C. Hernández-García, L. Plaja, A. Becker, A. Jaron-Becker, M. M. Murnane, H. C. Kapteyn, Bright coherent ultrahigh harmonics in the keV x-ray regime from mid-infrared femtosecond lasers. *Science* **336**, 1287–1291 (2012). doi:10.1126/science.1218497 Medline

16. N. Ishii, K. Kaneshima, K. Kitano, T. Kanai, S. Watanabe, J. Itatani, Carrier-envelope phase-dependent high harmonic generation in the water window using few-cycle infrared pulses. *Nat. Commun.* **5**, 3331 (2014). doi:10.1038/ncomms4331 Medline

17. S. L. Cousin, F. Silva, S. Teichmann, M. Hemmer, B. Buades, J. Biegert, High-flux table-top soft x-ray source driven by sub-2-cycle, CEP stable, 1.85-μm 1-kHz pulses for carbon K-edge spectroscopy. *Opt. Lett.* **39**, 5383–5386 (2014). doi:10.1364/OL.39.005383 Medline

18. F. Silva, S. M. Teichmann, S. L. Cousin, M. Hemmer, J. Biegert, Spatiotemporal isolation of attosecond soft X-ray pulses in the water window. *Nat. Commun.* **6**, 6611 (2015). doi:10.1038/ncomms7611 Medline

19. Z. H. Loh, M. Khalil, R. E. Correa, R. Santra, C. Buth, S. R. Leone, Quantum state-resolved probing of strong-field-ionized xenon atoms using femtosecond high-order harmonic transient absorption spectroscopy. *Phys. Rev. Lett.* **98**, 143601 (2007). doi:10.1103/PhysRevLett.98.143601 Medline

20. E. Goulielmakis, Z.-H. Loh, A. Wirth, R. Santra, N. Rohringer, V. S. Yakovlev, S. Zherebtsov, T. Pfeifer, A. M. Azzeer, M. F. Kling, S. R. Leone, F. Krausz, Real-time observation of valence electron motion. *Nature* **466**, 739–743 (2010). doi:10.1038/nature09212 Medline

21. M. Schultze, K. Ramasesha, C. D. Pemmaraju, S. A. Sato, D. Whitmore, A. Gandman, J. S. Prell, L. J. Borja, D. Prendergast, K. Yabana, D. M. Neumark, S. R. Leone, Attosecond

band-gap dynamics in silicon. *Science* **346**, 1348–1352 (2014). doi:10.1126/science.1260311 Medline

22. A. R. Attar, A. Bhattacherjee, S. R. Leone, Direct observation of the transition-state region in the photodissociation of CH_3I by femtosecond extreme ultraviolet transient absorption spectroscopy. *J. Phys. Chem. Lett.* **6**, 5072–5077 (2015). doi:10.1021/acs.jpclett.5b02489 Medline

23. K. Ueda, Y. Shimizu, H. Chiba, M. Okunishi, K. Ohmori, Y. Sato, E. Shigemasa, N. Kosugi, C 1s and F 1s photoabsorption and subsequent electronic decay of CH_4, CH_3F, CH_2F_2, CHF_3, and CF_4. *J. Electron Spectrosc. Relat. Phenom.* **79**, 441–444 (1996). doi:10.1016/0368-2048(96)02890-3

24. E. Hudson, D. A. Shirley, M. Domke, G. Remmers, A. Puschmann, T. Mandel, C. Xue, G. Kaindl, High-resolution measurements of near-edge resonances in the core-level photoionization spectra of SF_6. *Phys. Rev. A* **47**, 361–373 (1993). doi:10.1103/PhysRevA.47.361 Medline

25. D. M. P. Holland, A. W. Potts, A. B. Trofimov, J. Breidbach, J. Schirmer, R. Feifel, T. Richter, K. Godehusen, M. Martins, A. Tutay, M. Yalcinkaya, M. Al-Hada, S. Eriksson, L. Karlsson, An experimental and theoretical study of the valence shell photoelectron spectrum of tetrafluoromethane. *Chem. Phys.* **308**, 43–57 (2005). doi:10.1016/j.chemphys.2004.07.042

26. J. Creasey, H. M. Jones, D. M. Smith, R. P. Tuckett, P. A. Hatherly, K. Codling, I. Powis, Fragmentation of valence electronic states of CF_4^+ and SF_6^+ studied by threshold photoelectron-photoion coincidence spectroscopy. *Chem. Phys.* **174**, 441–452 (1993). doi:10.1016/0301-0104(93)80010-7

27. J. M. Garca de la Vega, E. San Fabián, Jahn-Teller effect and dissociation from the ground state of CF_4^+. *Chem. Phys.* **151**, 335–342 (1991). doi:10.1016/0301-0104(91)80019-E

28. J. L. Dehmer, D. Dill, S. Wallace, Shape-resonance-enhanced nuclear-motion effects in molecular photoionization. *Phys. Rev. Lett.* **43**, 1005–1008 (1979). doi:10.1103/PhysRevLett.43.1005

29. D. M. P. Holland, M. A. MacDonald, P. Baltzer, L. Karlsson, M. Lundqvist, B. Wannberg, W. von Niessen, An experimental and theoretical study of the valence shell photoelectron spectrum of sulphur hexafluoride. *Chem. Phys.* **192**, 333–353 (1995). doi:10.1016/0301-0104(94)00381-J

30. T. Suzuki, Femtosecond time-resolved photoelectron imaging. *Annu. Rev. Phys. Chem.* **57**, 555–592 (2006). doi:10.1146/annurev.physchem.57.032905.104601 Medline

31. H. J. Wörner, J. B. Bertrand, D. V. Kartashov, P. B. Corkum, D. M. Villeneuve, Following a chemical reaction using high-harmonic interferometry. *Nature* **466**, 604–607 (2010). doi:10.1038/nature09185 Medline

32. D. Polli, P. Altoè, O. Weingart, K. M. Spillane, C. Manzoni, D. Brida, G. Tomasello, G. Orlandi, P. Kukura, R. A. Mathies, M. Garavelli, G. Cerullo, Conical intersection dynamics of the primary photoisomerization event in vision. *Nature* **467**, 440–443 (2010). doi:10.1038/nature09346 Medline

33. H. J. Wörner, J. B. Bertrand, B. Fabre, J. Higuet, H. Ruf, A. Dubrouil, S. Patchkovskii, M. Spanner, Y. Mairesse, V. Blanchet, E. Mével, E. Constant, P. B. Corkum, D. M. Villeneuve, Conical intersection dynamics in NO_2 probed by homodyne high-harmonic spectroscopy. *Science* **334**, 208–212 (2011). doi:10.1126/science.1208664 Medline

34. N. Huse, T. K. Kim, L. Jamula, J. K. McCusker, F. M. F. de Groot, R. W. Schoenlein, Photo-induced spin-state conversion in solvated transition metal complexes probed via time-resolved soft X-ray spectroscopy. *J. Am. Chem. Soc.* **132**, 6809–6816 (2010). doi:10.1021/ja101381a Medline

35. M. Ekimova, W. Quevedo, M. Faubel, P. Wernet, E. T. J. Nibbering, A liquid flatjet system for solution phase soft-x-ray spectroscopy. *Struct. Dyn.* **2**, 054301 (2015). doi:10.1063/1.4928715 Medline

36. H. Dossmann Soldi-Lose, G. A. Garcia, L. Nahon, B. K. de Miranda, C. Alcaraz, Comprehensive vacuum ultraviolet photoionization study of the CF_3(●) trifluoromethyl radical using synchrotron radiation. *J. Chem. Phys.* **136**, 204304 (2012). doi:10.1063/1.4719529 Medline